Organ- and function-specific anatomical organization and bioelectronic modulation of the vagus nerve

Naveen Jayaprakash[1], Viktor Toth[1], Weiguo Song[1], Avantika Vardhan[1], Todd Levy[1], Jacquelyn Tomaio[2], Khaled Qanud[1], Ibrahim Mughrabi[1], Yao-Chuan Chang[1], Moontahinaz Rob[3], Anna Daytz[4], Adam Abbas[5], Jason Ashville[6], Anna Vikatos[7], Umair Ahmed[1], Zeinab Nassrallah[4], Bruce Volpe[1], Kevin J. Tracey[1], Yousef Al-Abed[1], Timir Datta-Chaudhuri[1], Larry Miller[1], Mary Barbe[8], Sunhee Lee[1], Theodoros Zanos[1], Stavros Zanos*[1]

[1] Feinstein Institutes for Medical research, Manhasset, New York. [2] The City University of New York, New York. [3] Northwell Health, New York .[4] Donald and Barbara Zucker School of Medicine at Hofstra/Northwell, Hempstead, New York. [5] University at Buffalo Jacobs School of Medicine and Biological Sciences, Buffalo, New York. [6] NYIT College of Osteopathic Medicine, Glen Head, New York. [7] The Bronx High School of Science, Bronx, NY. [8] Temple University, Philadelphia, Pennsylvania. *Corresponding author. Email: szanos@northwell.edu

Abstract

Afferent and efferent fibers in the vagus travel inside nerve fascicles and form branches to innervate organs and regulate organ functions. The organization of fibers and fascicles in the vagus trunk, with respect to the functions they mediate and the organs they innervate, remains largely unknown. Accordingly, it is unknown whether that anatomical organization can be leveraged by bioelectronic devices for function- and organ-specific neuromodulation. To characterize the microscopic functional anatomy of the vagus we developed a pipeline consisting of micro-computed tomography-based morphometry of fascicles and quantitative immunohistochemistry of single fibers. We found that, in the swine vagus, fascicles form clusters specific to afferent and efferent functions, increasingly separated in the rostral direction, and other clusters specific to the innervated organs, including larynx, lungs and heart, increasingly separated in the caudal direction. Large myelinated and small unmyelinated efferents have small counts, cover large area of the nerve, and are limited to specific fascicles; small unmyelinated afferents have large counts, cover small area, and are uniformly distributed across fascicles. To test whether fiber populations can be selectively modulated, we developed a multi-contact cuff electrode that observes the fascicular vagus anatomy. Targeting of different nerve sub-sections evokes compound action potentials from different fiber types and elicits differential organ responses, including laryngeal muscle contraction, cough reflex, and changes in breathing and heart rate. Our results indicate that vagus fibers are spatially clustered according to functions they mediate and organs they innervate and can be differentially modulated by spatially selective nerve stimulation.

Introduction

The autonomic nervous system maintains physiological homeostasis in organs and systems through an interconnected network of neural reflexes. Autonomic reflexes are comprised of sensory neurons that detect changes in physiological parameters, and motor neurons that modulate organ functions in response to sensed physiologic changes. With its large number of afferent (sensory) and efferent (motor) fibers, the vagus is the main conduit for bidirectional communication between the brain and body organs and a component of several cardiopulmonary, gastrointestinal and neuroimmune reflexes. In the human vagus, afferent and efferent fibers are arranged in fascicles, longitudinal bundles within the nerve separated by connective tissue [1, 2] [3]. At different levels of the cervical, thoracic and abdominal vagus, afferent and efferent fibers enter and leave the fascicles and converge to form nerve branches, which in turn provide sensory and motor innervation to organs of the neck, chest and abdomen [4, 5]. Even though much is known about the macroscopic and microscopic anatomy of the vagus, the spatial organization of fascicles within the nerve, as it relates to the innervated visceral organs, and of fibers, as it relates to the afferent and efferent functions they mediate, remains unknown. For example, it is unknown whether fibers and fascicles are organized randomly in the vagus or are spatially segregated according to which organ they project or according to which function they mediate, similar to the fascicular somatotopy of other peripheral nerves [6].

The spatial organization of fibers in the human vagus has implications for bioelectronic devices seeking to modulate nerve activity to treat diseases of the brain and peripheral organs in which autonomic reflexes are implicated, such as heart failure [7], inflammatory bowel disease [8] and rheumatoid arthritis [9]. Even though vagus nerve stimulation (VNS) devices aim to modulate autonomic functions in specific organs, current devices deliver electrical stimulation all around the nerve, without considering the spatial organization of fascicles and functional fiber types [1, 10-13]. If known, the fascicular and fiber organization of the vagus could be leveraged by appropriately designed electrode devices to deliver organ- and function-selective VNS. Anatomically- and functionally-selective VNS could reduce clinically significant side-effects of vagus neuromodulation therapies [11, 14], expand those therapies to disease indications involving organs that are currently not targeted [15, 16], and allow the study of autonomic reflexes by targeting specific fiber populations in the vagus.

In this study, we developed a quantitative anatomical pipeline to characterize the arrangement of vagus nerve fibers, with regard to functional fiber types, fascicles, and innervated organs in the swine, the preferred animal model for the human vagus [1, 3]. We discovered rich anatomical organization of fibers within the vagus, with fascicles and fibers clustered in separate groups with regard to the specific functions they mediate and the organs they innervate. We then developed a multi-contact cuff electrode device that observes that spatial arrangement in the cervical vagus and used it to deliver spatially selective VNS. We found that by targeting different sub-sections of the nerve we are able to evoke action potentials from different functional types of nerve fibers and elicit differential responses from organs innervated by the vagus.

Results

Fascicles form organ-specific clusters along the vagus

The vagus in swine is highly fascicular, with 40-50 fascicles of varying sizes in the cervical region [Suppl. Figure S1]. Branches derived from the cervical and thoracic vagus provide sensory and motor innervation to visceral organs [5], including the larynx and pharynx, through the superior and recurrent laryngeal nerves [17], the heart, through the cardiac branch [5, 18], and the lower airways and lungs, through the bronchopulmonary branches [19]. To understand the spatial arrangement of fascicles with respect to the formation of vagus branches, we performed high resolution micro-computed tomography (μCT) imaging of the vagus nerve trunk, from the nodose ganglion, rostrally, to the lower thoracic portion of the nerve, caudally. Fascicles with any visible contribution to the formation of a vagus branches were manually annotated at individual sections taken through the branching point (Suppl. Figures S2, S3, S4) and were considered to project to the corresponding organ (Figure 1A). The longitudinal trajectories of those fascicles were then tracked in all μCT images along the length of the vagus rostrally with the use of an automated image segmentation algorithm.

We found that fascicles contributing to the bronchopulmonary (BP) branch form a cluster close to the entry level (yellow fascicles, Figure 1B, panels x and w; and Figure 1C, panels r and q); bronchopulmonary fascicles remain clustered for several centimeters rostrally (Figure 3B, panels v-s; Figure 3C, panels p-o). The recurrent laryngeal nerve (RNL) joins the trunk by contributing another cluster of fascicles (red fascicles; Figure 1B, panels r-q; Figure 1C, panels n-m). Some of those fascicles ascend in parallel to the BP cluster and some merge with it, in a “composite” BP-RLN cluster (orange fascicles; Figure 1B, panels p-o; Figure 1C, panels m-l). Both BP and RLN fascicles disappear within a few centimeters and are replaced by a cluster of combined BP-RLN fascicles which runs rostrally along the upper thoracic (Figure 1B, panel n) and the cervical vagus (Figure 1C, panel l). The cardiac branch joins the vagus trunk rostrally to the RLN entry and forms a separate cluster of fascicles (blue fascicles; Figure 1B, panel o; Figure 1C, panel l). Some of the cardiac fascicles maintain their separate trajectories all the way through the upper thoracic and cervical vagus (Figure 1B, panels l-d; Figure 1C; panels k-d) and some merge with the composite BP-RLN fascicles to form a larger composite cluster of BP-RLN-cardiac (green fascicles; Figure 1B, panels m and above; Figure 1C, panels e and above). Many of the combined BP-RLN-cardiac fascicles terminate in the nodose ganglion, and some of them bypass it (Figure 1B, panels b, a; Figure 1C, panels b, a). Fascicular branching, where one fascicle branches to from two fascicles, or fascicular merging, where two fascicles merged to form one fascicle is observed throughout the length of the nerve (Suppl. Figure S5, and Supplementary video 1). <u>These findings indicate that fascicles in the thoracic and cervical vagus trunk form spatially distinct organ-specific clusters close to the levels of entry of branches to those organs; clusters progressively merge into larger composite clusters in the caudal to rostral direction</u>.

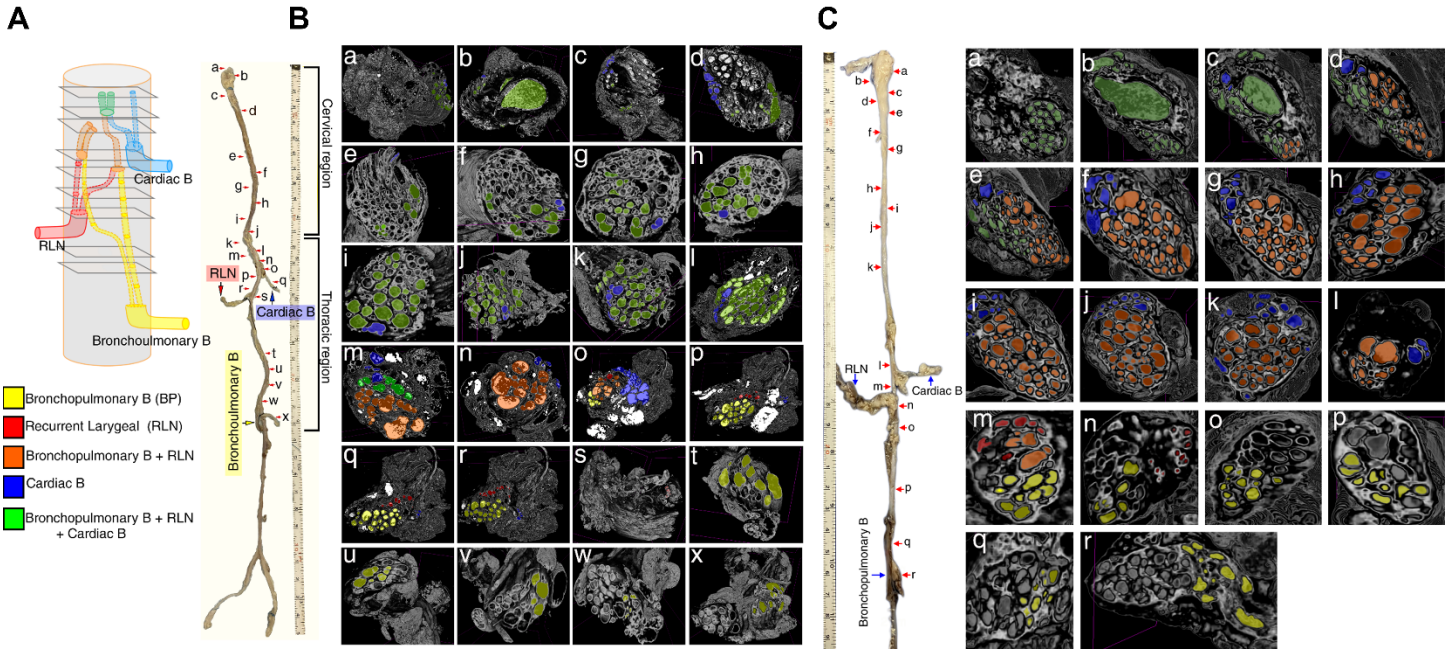

Figure 1. Fascicles form organ-specific clusters along the vagus. (A) Schematic showing a segment of the vagus trunk with 3 branches joining it (bottom to top): bronchopulmonary (BP, yellow), recurrent laryngeal nerve (RLN, red), cardiac branch (blue). The trajectories of fascicles contributing to each branch were traced rostrally inside the trunk, even after they merged with other fascicles to form "combined" fascicles: BP and RLN (orange), BP, RLN and cardiac (green). (B) Macroscopic structure of an intact right vagus trunk, from the nodose ganglion to the lower thoracic level (left). On the right, multiple micro-computed tomography sections through the trunk are shown (panels a-x), with fascicles contributing to each of the identified branches or combinations of branches shaded in the corresponding colors. (C) Macroscopic and fascicular structure of an intact left vagus trunk from a second animal.

Fascicles form separate afferent and efferent clusters along the vagus

To understand the spatial arrangement of fascicles with respect to the afferent or efferent function, we analyzed the μCT images in the opposite direction, from rostral to caudal: fascicles that terminate in the nodose ganglion were considered (primarily) afferent and those that bypass the nodose ganglion were considered (primarily) efferent (Figure 2A, panels a, b). By tracking those fascicles caudally, we found that afferent and efferent fascicles form separate clusters throughout the cervical vagus (Figure 2A, panels a to i). To examine whether the separation of afferent and efferent fascicles persists at the single fiber level, we performed immunohistochemistry (IHC) in sections through the nodose ganglion, mid-cervical and thoracic region (Figure 2B, Suppl. Figure S6 and S7).

At the nodose ganglion level (Figure 2B, panel a), ChAT-positive (ChAT+) fibers, indicative of efferent function, were almost absent (Figure 2B, panel b) but were frequently observed in fascicles outside of the nodose ganglion (Figure 2B, panel c). On the other hand, Nav1.8-positive (Nav1.8+) sensory neurons are found in the nodose ganglion as pseudo-unipolar cells (Figure 2B, panel d; and Suppl. Figure S8); smaller numbers of Nav1.8+ clusters were observed in fascicles outside of the nodose ganglion (Figure 2B, panel e). At the mid-cervical region (Figure 2B, panel f), separate clustering of fascicles rich in ChAT+ fibers (Figure 2B, panel g) from those poor in ChAT+ fibers was observed (Figure 2B, panel h, Suppl. Figure, S9), whereas such separation was absent in the thoracic region (Suppl. Figure, S10); Nav1.8+ fibers were seen in both fascicle clusters (Figure 2B, panel i & j). <u>These findings indicate that primarily afferent and primarily efferent fascicles form spatially distinct clusters in the upper and mid-cervical trunk of the vagus; the clusters become progressively less separated moving from the rostral to caudal directions, and in the thoracic region the afferent-efferent separation no longer exists.</u>

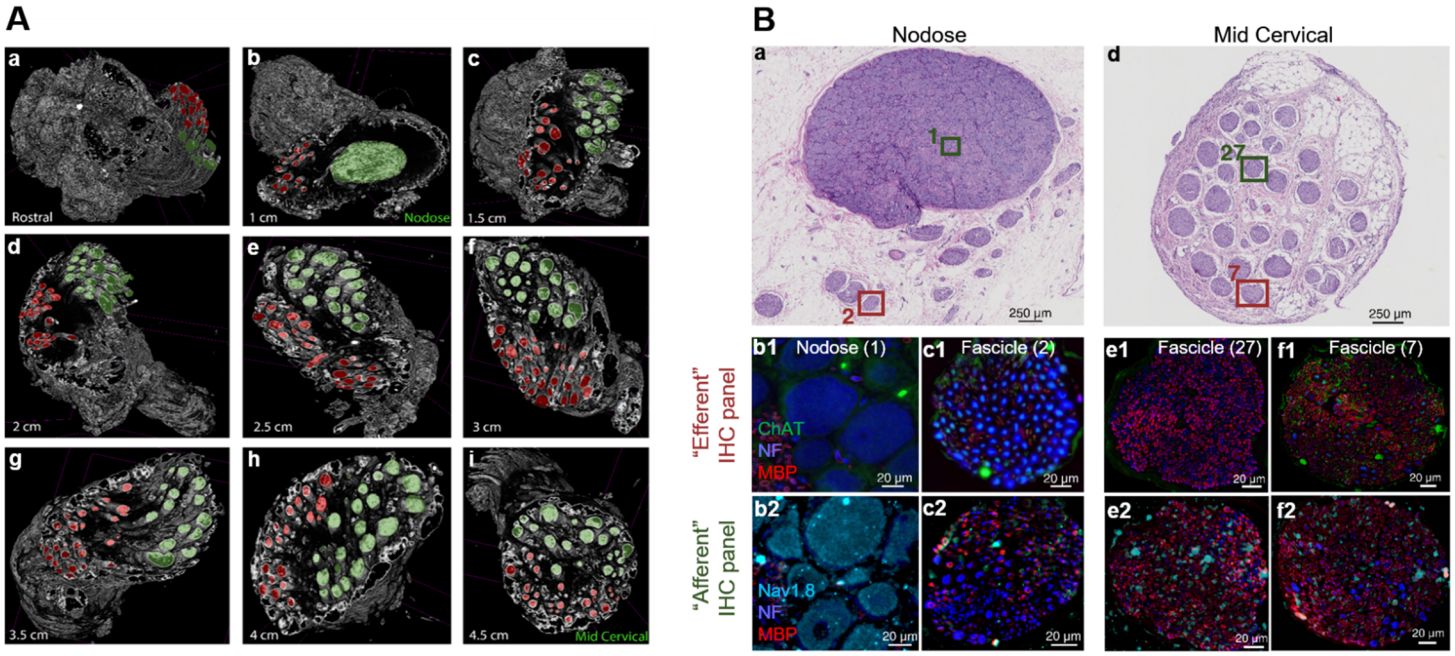

Figure 2. Afferent and efferent fascicles form clusters along the vagus. (A) Micro-computed tomography imaging of the cervical region of an intact right vagus trunk, from the nodose ganglion to the mid-cervical level. Fascicles that originate in the nodose ganglion were considered primarily afferent (shaded green), and those that "by-passed" the nodose were considered primarily efferent (shaded red). Panels (a-i) show the trajectories of afferent and efferent fascicles in consecutive sections through the cervical vagus, at different levels (shown in cm from the rostral end of the sample). (B) Imaging of afferent and efferent fibers in primarily afferent and primarily efferent fascicles. (a) H&E section at the level of the nodose ganglion. An area inside the ganglion (1) and a primarily efferent fascicle (2) are selected. (b1) Nodose area stained with an "efferent" panel of antibodies for immunohistochemistry (IHC), consisting of anti-neurofilament antibody (NF, blue) that labels nerve fibers, anti-myelin basic protein antibody (MBP, red) that labels myelin, and choline-acetyl-transferase (ChAT, green) that labels efferent, cholinergic, fibers. (b2) The same nodose area stained with an "afferent" IHC panel, consisting of NF, MBP and anti-Nav1.8 antibody (cyan) that labels afferent fibers. (c1) Fascicle (2) stained with an efferent IHC panel. (c2) Fascicle (2) stained with an afferent IHC panel. (d) H&E section at the mid-cervical level. A primarily afferent (27) and a primarily efferent fascicle (7) are selected. The 2 fascicles are stained with an efferent (e1 and f1, respectively) and an afferent IHC panel (e2 and f2, respectively).

Functional types of nerve fibers are specifically organized across and within fascicles in the cervical vagus

The human and swine vagus contain fibers of several types, including myelinated and unmyelinated afferents and efferents [2, 11, 12]. Large myelinated efferents (Aα-type) provide somatic innervation to laryngeal muscles [19, 20]; smaller myelinated efferents (B-type) are typically cholinergic and provide parasympathetic innervation to visceral organs, like the heart and the GI tract [20]. Large myelinated afferents (Aβ -type) provide sensation to the pharyngeal and laryngeal mucosa [21-23], ([24-26]) whereas smaller ones (Aδ-type) project to mechanical and chemical sensory receptors in visceral organs [27-30], ([31-34]. Finally, unmyelinated (C-type) efferents are primarily sympathetic fibers to visceral organs [35-37] ([23, 30, 35], whereas C-type afferents provide nociception, mechanical and chemical sensation to visceral organs [22, 28, 29, 38] ([25, 32, 33, 39]. To understand the spatial organization of vagus fibers in the cervical region, the most common anatomical location for stimulation electrodes, we developed a quantitative IHC pipeline, consisting of IHC staining, imaging and automated fiber segmentation, feature extraction and analysis of fibers. Based on the expression pattern of fiber-specific IHC markers, we classified each fiber as myelinated efferent (MEff, Figure 3A,a), myelinated afferent (MAff, Figure 3A, b), unmyelinated efferent (UEff, Figure 3A, c) or unmyelinated afferent

(UAff, Figure 3A, d). For UAff fibers in particular, that do not stain for neurofilament (NF), we considered individual Nav1.8+ fibers clustered in Remak bundles [40, 41], surrounded by the cytoplasm of non-myelinating S100+ Schwann cells (Figure 3B; Suppl. figure S11).

	A	B	C	D	E	F	G	H	I				
	Fiber type	Erlanger Gasser class.	Side	% Fiber area in nerve, mean [range]	Fiber count in nerve, mean [range]	% Fiber count in nerve, mean [range]	% Fiber area in fascicle, mean [range]	Fiber count in fascicle, mean [range]	Fiber type features				
									NF	MBP	ChAT	Nav1.8	Diameter (μm), mean (IQR)
1	Myel. eff. (MEff)	Aα, Aγ & B	L R	33 [28–35] 31 [15–43]	14.8K [12.7–16.6] 14.6K [4.9–21.4]	4.2 [2.7–6.4] 5.1 [0.7–8.7]	29 [0–83] 29 [0–83]	335 [0–2,419] 403 [0–1,879]	+	+	+	NA	3.47 (1.46)
2	>10 μm	Aα	L R	1.9 [0.4–4.6] 1.8 [0.5–4.5]	52 [12–130] 54 [12–127]	0.01 [0–0.03] 0.01 [0–0.02]	1.25 [0–27] 1.20 [0–19]	1.2 [0–33] 1.5 [0–21]	+	+	+	NA	15.7 (5.93)
3	<3 μm	B	L R	15 [12–20] 16 [4–27]	11.6K [9.5–13.5] 11.8K [3.4–18.7]	3.3 [2.0–5.2] 4.2 [0.5–7.6]	13.8 [0–48] 14.5 [0–57]	14 [0–48] 32 [0–57]	+	+	+	NA	3.06 (1.05)
4	Myel. aff. (MAff)	Aβ & Aδ	L R	52 [50–56] 58 [48–74]	34.0K [29.7–37.6] 28.7K [25.8–31.4]	9.1 [7.8–11.2] 8.7 [5.2–10.5]	54 [0–86] 59 [12–92]	766 [0–2,753] 790 [20–3,401]	+	+	–	NA	3.10 (1.42)
5	>5 μm	Aβ	L R	3.6 [1.2–5.7] 14 [1.7–36]	409 [163–623] 1,348 [178–3,109]	0.10 [0.06–0.14] 0.30 [0.02–0.59]	3.1 [0–20] 10 [0–54]	9 [0–56] 37 [0–510]	+	+	–	NA	8.49 (2.98)
6	2-5 μm	Aδ	L R	40 [37–42] 37 [33–42]	20.4K [17.7–22.4] 17.6K [13.9–21.2]	5.5 [4.7–6.8] 5.3 [3.2–7.1]	41 [0–72] 40 [0–83]	41 [0–72] 48 [0–84]	+	+	–	NA	3.72 (1.21)
7	Unmyel. eff. (UEff)	C-Symp.	L R	6.9 [5.1–8.8] 4.7 [2.9–7.4]	21.8K [15.1–25.7] 15.8K [10.8–23,3]	6.3 [3.1–9.8] 4.9 [2.4–7.8]	8.9 [0.6–54] 6.6 [0.7–35]	492 [9–3,084] 434 [26–1,626]	+	–	–	NA	1.83 (0.78)
8	Unmyel. aff. (UAff)	C-Aff.	L R	7.6 [5.1–10.2] 6.3 [5.1–7.9]	315K [190.0–414.0] 294K [186.0–470.0]	80 [72–86] 81 [75–91]	7.2 [1–28] 5.3 [0–16]	7,117 [42–63,519] 8,088 [0–77,927]	–	–	NA	+	0.55 (0.32)

Table I. Fiber counts and associated areas of coverage (relative and absolute) of different fiber types in the cervical vagus. Different fiber types (rows 1-8) according to criteria used in our pipeline (A) and corresponding fiber types according to Erlanger-Gasser classification (B). (C) Nerve side (left or right). (D) Percentage of fiber-covered area in the entire nerve corresponding to a given fiber type; shown is mean and range across 8 nerves. (E) Absolute fiber count of given fiber type in the entire nerve. (F) Percentage of given fiber type among all fibers in the whole nerve. (G) Percentage of area covered by given fiber type in single fascicles; mean [range] across all fascicles, of all nerves. (H) Absolute count of given fiber type in single fascicles. (I) Fiber type-specific features used in our pipeline to classify single fibers: positive (+) or negative (-) in NF stain, MBP (myelin basic protein) stain, ChAT (choline-acetyl-transferase) stain, and Nav1.8 stain. Measured diameters for each fiber type (in μm, mean and interquartile range).

Overall, we counted 200-450K individual fibers in each nerve, with more than 80% being of the UAff type; however, UAff fibers take up less than 10% of the total fiber-covered area in the nerve (table I). Myelinated fibers, MAff and MEff, despite representing less than 15% of total fiber count, take up 65-85% of fiber-covered area (table I; and Suppl. Figure S12). There is substantial variability in fiber counts and in the area they cover across fascicles, for all fiber types. In both left and right cervical vagus, fascicles with large MEff fiber counts are clustered together on one side of the nerve (Figure 3C, a1 and a2), in agreement with our μCT and IHC findings (Figure 2). The few, larger Aα-type fibers were concentrated in a few fascicles within the cluster (Figure 3C, bottom left in a1 and a2), whereas the smaller, B-type fibers were more uniformly distributed within the fascicles of the cluster (Figure 3C, bottom right in a1 and a2). Fascicles with large MAff fiber counts were clustered in the opposite, side of the nerve (Figure 3C, b1 and b2). MAff fibers include intermediate size Aδ-type fibers, uniformly distributed within the cluster (Figure 3C, bottom left in b1, b2), and the fewer, larger Aβ-type fibers, concentrated in a subset of fascicles in the cluster (Figure 3C, bottom right in b1, b2). The fascicular arrangement of UEff fibers parallels that of MAff and opposes that of MEff fibers (Figure 3C, c1 and c2). Indeed, counts of UEff are negatively correlated with those of MAff fibers (Figure 3D, a) and positively correlated with those of MEff fibers (Figure 3D, b). UAff fibers are present in all fascicles, even though their fiber count varied between 50% and >80% (Figure 3C, d1 and d2). Fiber distribution fascicular maps from additional nerves are given in Suppl. Figure S13. More than 50% of all fibers in the nerve, independently of fiber type, lie within 500 μm from the epineurium (Suppl. Fig. S14 & S15), indicating that the majority of vagus

fibers can potentially be activated by epineurial cuff electrode devices. The clustering of UEff fibers together with MAff and away from MEff fibers is observed even at the sub-fascicular level: sectors of a fascicle with high UEff counts tend to have low MEff counts (Figure 3E, a) and high MAff counts (Figure 3E, b). Within sub-fascicular sectors, fibers of the same type tend to cluster together (main diagonal of Figure 3E, c). No spatial interaction was observed between other fiber types within the fascicle (Suppl. Figure S16) Taken together, these findings indicate that despite the variability in the fiber composition of fascicles in the cervical vagus, there are consistent patterns. MAff and MEff fibers are organized in separate clusters of fascicles. UEff fibers co-localize with MAff rather than MEff fibers, in whole fascicles, and in sub-fascicular sectors. UAff fibers are widely and relatively uniformly distributed across and within fascicles.

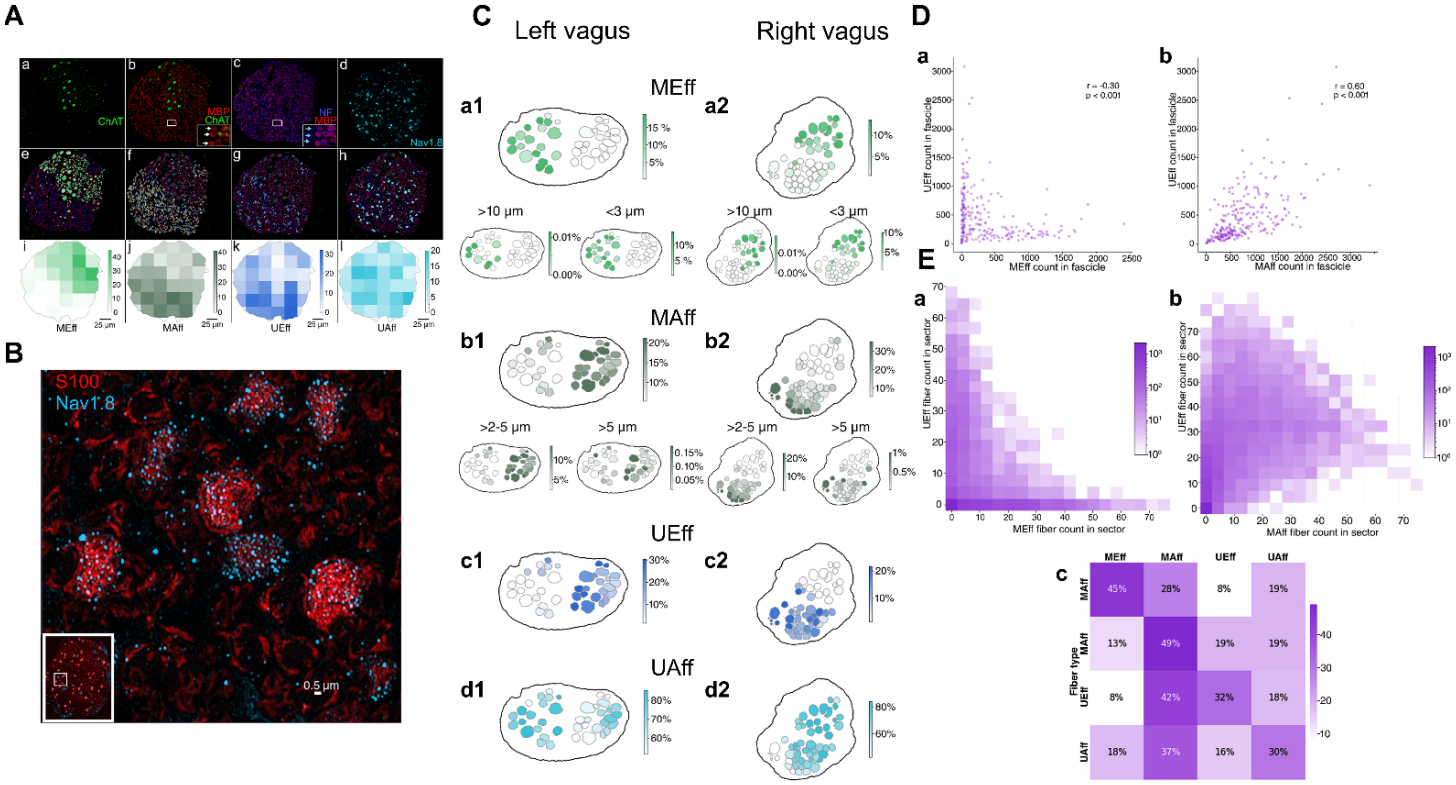

Figure 3. Functional nerve fiber types are specifically arranged in the cervical vagus nerve. (A) A large-scale immunohistochemistry (IHC) and analytical pipeline was used to image, identify, characterize and classify all fibers in every fascicle. (a) ChAT+ fibers (Suppl. Figure S17) that were also NF+ and MBP+ (NF and BMP channels are not shown for clarity) were classified as myelinated efferents (MEff). (b) NF+ and MBP+ fibers that were also ChAT- were classified as myelinated afferents (MAff); white arrows point to single MAff fibers in inset. (c) NF+ and BMP- fibers were classified as unmyelinated efferents (UEff); blue arrows point to single MEff fibers in inset. (d) Nav1.8+ and MBP- fibers were classified as unmyelinated afferents (UAff). Unmyelinated afferent fibers did not stain for NF (Suppl. Fig. S18). (panels e-h) Individual fibers of each type were identified, and their features (e.g. size) and location in the fascicle were extracted. This allowed us to assess for different fiber types statistics of fiber counts, the area they cover and distributions across fascicles. (panels i-l) Local density values of each fiber type were extracted from fiber counts and locations, and projected on a fascicle using a color scale. This allowed us to assess within-fascicle arrangement of different fiber types. (B) IHC imaging of UAff fibers in a section of a nerve fascicle. Stains for Nav1.8, specific to afferent fibers, and S100, specific to non-myelinating Schwann cells, are shown superimposed to reveal several Remak bundles, within which individual UAff fibers are surrounded by the cytoplasm of Schwann cells. Inset shows the entire nerve fascicle. (C) Counts of fibers of different types in the fascicles in a section from the left and the right cervical vagus trunk of the same animal. (a1) Counts of MEff fibers across fascicles of the left vagus, as percentage of total number of fibers in each fascicle; percent counts represented by a color intensity scale. Top: Counts of all MEff fibers, independently of diameter. Bottom left: Counts of MEff fibers with diameter>10µm (Aα-type). Bottom right: Counts of MAff fibers with diameter<3µm (B-type). (a2) Same as a1, but for the right vagus. (b1) Counts of MAff fibers across fascicles of the left vagus. Top: for all MAff fibers; bottom left:

for MAff fibers with diameters 2-5μm (Aβ-type); bottom right: for MAff fibers with diameters >5μm (Aδ-type). (b2) Same as b1, but for the right vagus. (c1) Counts of UEff fibers across fascicles of the left vagus, and (c2) of the right vagus. (d1) Counts of UAff fibers across fascicles of the left vagus, and (d2) of the right vagus. (D) Distinct relationships in co-localization of different fiber types across fascicles. (a) Anti-correlated counts of MEff fibers in a fascicle (abscissa) vs. counts of UEff fibers in the same fascicle (ordinate). Each point represents a single fascicle. Shown are data from all fascicles in the cervical vagus of 4 animals (8 nerves). (b) Correlated counts of MAff and UEff fibers. (E) Distinct relationships of co-localization of different fiber types within fascicles. (a) Counts of MEff and UEff fibers within a 30-μm-square fascicular sector in all analyzed fascicles. The color intensity of each pixel represents the frequency of the specific combination of MEff-UEff fiber counts: the lighter the color, the less frequent that combination is across sectors. Shown are data from all sectors within all fascicles, from all nerves. (b) Correlated counts of MAff and UEff fibers within a 30-μm-square sector. (c) Joint probability of co-localization of different fiber types within a 30-μm-square sector. In each row, color intensity and percentage values represent the probability of finding a fiber of each of the 4 types in the immediate vicinity of the fiber type represented by that row.

Spatially selective vagus nerve stimulation differentially activates organ- and function-specific fibers

Activation or blocking of different efferent and afferent fiber populations by electric fields generated by bioelectronic devices determines end-organ effects of vagus neuromodulation therapies. Having demonstrated that vagus fibers have an organ- and function-specific arrangement, we next sought to test whether spatially selective VNS can differentially activate fibers innervating specific organs, as well as distinct functional fiber types. Given that intraneural electrodes may create increased risk of injury [42, 43], and that >50% of fibers lie within 500 μm from the epineurium (Suppl. Fig. S14 & S15), we developed an epineurial nerve cuff electrode. The cuff included 8 circumferentially placed contacts and 2 ring-shaped return contacts (Figure 4A). The 8-contact electrode design was chosen because, in simple computer simulations of 2-D geometric representations of vagus nerves (Suppl. Figure S19A), it attains significantly higher overall efficacy compared to designs with fewer contacts (Suppl. Figure S19B,a), with the same selectivity as other designs (Suppl. Figure S19B, b); finally it is compatible with the fascicular anatomy of the human cervical vagus (Suppl. Figure S19B, c).

Stimulation through different contacts in the multi-contact electrode produces different physiological responses from the heart, vessels, lungs and laryngeal muscles (Figure 4B). Stimulation elicits evoked compound action potentials (eCAPs), which reflect the direct activation of fibers; differential activation of fast fibers, with a conduction velocity consistent with Aα/β-type fibers; and of slow fibers, with a conduction velocity consistent with Aδ/B type-fibers, is also observed, depending on which contact is used for stimulation (Figure 4C). To characterize the physiological and fiber responses to stimulation through each of the 8 electrode contacts, threshold intensities for eliciting different organ responses were determined for each contact [44] and those thresholds were plotted on a map of the “directionality” of individual organ responses (Figure 4D). Responses from different organs have different thresholds, and those thresholds depend on which contact is used for stimulation, resulting in asymmetric directionality maps that are different for each organ response (Figure 4D). Similarly, amplitudes of fast and slow fiber activity in eCAPs depend on the stimulated contact (Figure 4E). Graded organ responses and amplitude of fibers mediating them are observed at a range of stimulus intensities, resulting in parallel recruitment curves (Figure 4F). By aligning polar plots in individual animals by the contact with the minimum heart rate threshold and normalizing responses between a minimum and maximum value, we compiled average maps of the directionality of organ responses across animals (Figure 4G). The radial location on the nerve associated with the lowest heart rate threshold on a single nerve basis (heart-specific location) was arbitrarily placed at 12 o’clock (90° angle). The vector sum of heart rate thresholds points towards the location with the greatest threshold and away from the “heart-specific” nerve location which, when averaged across 12 animals, lies at an angle of 103° (Figure 4G, a). The lung-specific nerve location lies at an angle of 128° (Figure 4G, b) and the larynx-specific location lies at an angle of 75° (Figure 4G, c). The

directionality map for blood pressure response is similar to that for heart rate response (Figure 4G,d). Similarly, by aligning polar plots in individual animals by the contact with the maximum fast fiber amplitude, arbitrarily placed at 12 o'clock (90° angle), and normalizing, we compiled average maps of the directionality of fast and slow fiber response amplitudes across animals. The fast fiber-specific location of the nerve lies at 95° (Figure 4G, a), and the slow fiber-specific location at 142° (Figure 4G, b). The larynx-specific nerve location, which was determined by measuring fast fiber-mediated laryngeal EMG responses, lies 53° clockwise to the lung-specific location, which was determined by measuring slow fiber-mediated breathing rate responses. This angular separation is similar to that between the fast fiber- and slow fiber-specific locations on the nerve, which are separated by 47° clockwise. To test whether spatial selectivity is consistent across multiple days, we performed chronic vagus implants with the multi-contact cuff electrode device in 2 animals. We found that threshold intensities for eliciting the cough reflex, whose sensory arc is mediated by MAff fibers innervating the laryngeal and pharyngeal mucosa, are asymmetrically distributed around the nerve and, despite the gradual increase in thresholds, the overall shape of the spatial distribution is maintained for up to 3 weeks post-implantation (Suppl. Figure S20). Together, these findings indicate that the spatial organization of afferent and efferent and organ-specific fascicles and fibers in the vagus can be leveraged with a multi-contact cuff electrode to deliver spatially specific nerve stimulation, as organ and fiber responses depend on the location of the stimulated contact.

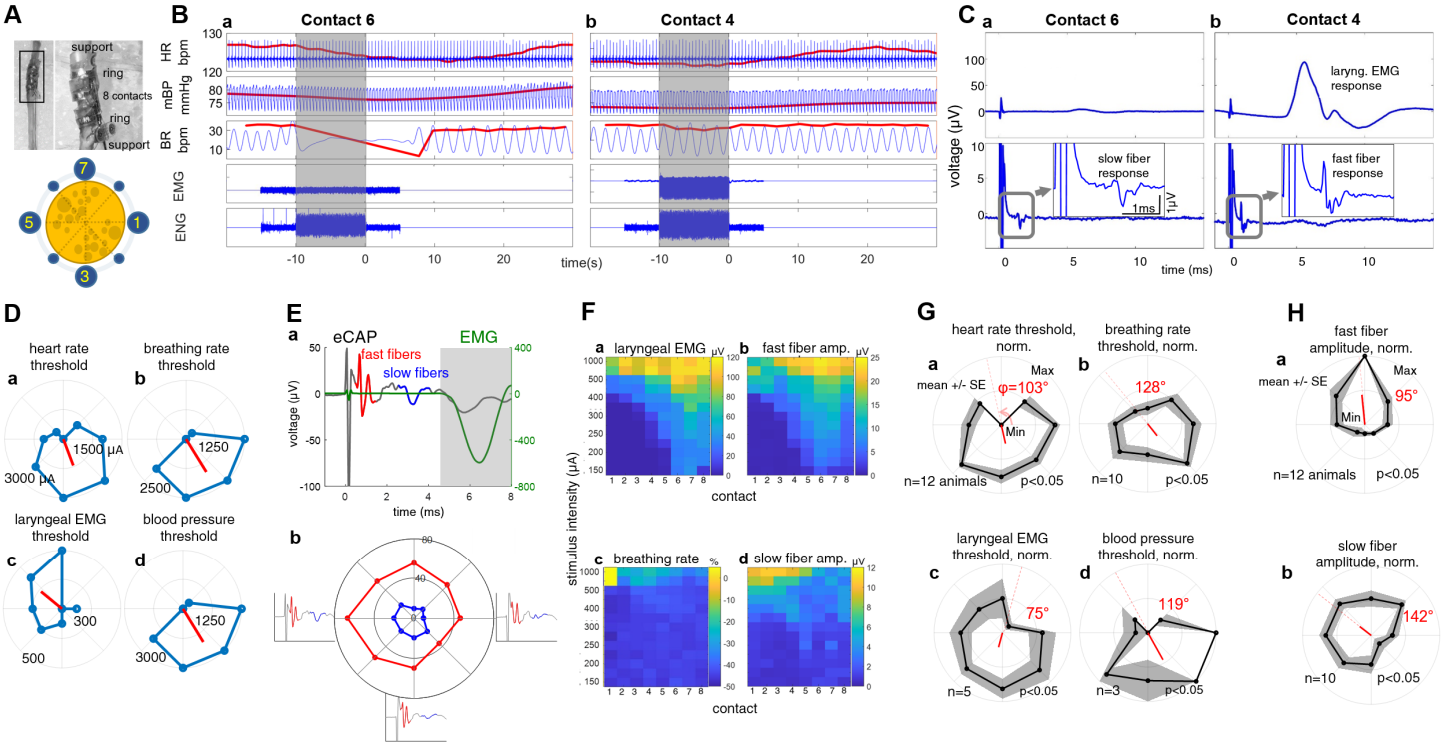

Figure 4. Spatially selective vagus nerve stimulation differentially activates organ- and function-specific fibers. (A) Helical multi-contact cuff electrode placed on the cervical vagus (left); the cuff is comprised of 2 outer support loops, 2 ring-shaped contacts, and 8 small square contacts, circumferentially placed around the nerve (right). (B) (a) Cardiovascular, respiratory and laryngeal physiological responses to a stimulus train (shaded area) through one of the 8 contacts (contact 6) include drop in heart rate (HR), a moderate drop in mean blood pressure (BP) and slowing of breathing rate (BR); at the same time, minimal evoked laryngeal muscle activity (EMG) and strong evoked responses in the nerve potential (ENG) were observed. (b) Responses to the same stimulus train delivered through a different contact (contact 4) included minimal drop in HR, BP and BR but strong laryngeal EMG. (C) (a) Evoked laryngeal EMG (top) and compound nerve action potential (eCAP, bottom) triggered by stimuli in the train delivered to contact 6. No EMG is generated and the eCAP shows a response at a latency consistent with slow A-fiber activation. (b) EMG and eCAP

triggered by stimuli delivered to contact 4; EMG response and a short latency eCAP, consistent with fast A-fiber activation, are observed. (D) Threshold intensities for different physiological responses determined for each of the 8 different contacts in the multi-contact cuff electrode: (a) threshold for HR response, (b) BR threshold, (c) laryngeal EMG threshold, (d) BP threshold. Threshold was defined as the minimum intensity of a stimulus train (200 μs pulse width, 30 Hz) that produces a change of 5-10% in the corresponding physiological variable. Shown are averages of thresholds determined from 3-5 trains in each contact, all in the same animal. (E) Fast and slow fiber responses in eCAPs elicited from each of the 8 contacts. (a) Evoked EMG activity. (b) eCAP activity with latency-based classification of fast (red trace) or slow fiber responses (blue trace). (c) Fast and slow fiber amplitudes on each of the 8 contacts. (F) Physiological responses and eCAPs mediating them have different recruitment curves from different contacts. (a) Amplitude of laryngeal EMG is shown for different stimulation contacts (abscissa) and at different intensities (ordinate), represented by the color scale (dark blue: 0μV; bright yellow: 120μV). (b) Same for amplitude of fast fiber response in the eCAP; fast fibers (e.g. Aα) mediate efferent signaling to laryngeal muscles. (c) Same for the magnitude of breathing response, quantified as % change in BR. (d) Same for amplitude of slow fiber response in the eCAP; slow fibers (e.g. Aδ) mediate afferent signaling to the brain that, through a reflex mechanism (Herring-Breuer reflex) slows down or arrests breathing. (G) Spatial distributions of normalized threshold intensities and associated “preferred directions” for physiological responses across animals. (a) Average (+/-SE) normalized HR threshold in 12 animals. The contact with minimum HR threshold in each animal is placed at 12 o’clock direction (origin of polar plot); outer circle of polar plot represents the maximum HR threshold for each animal. p value represents statistical significance of 1-way ANOVA (dependent variable: threshold, independent variable: direction of contact). Red line represents the vector sum of preferred directions of distributions from all animals; it points towards the side of the nerve with the greatest threshold (and therefore the *least* selective for the corresponding physiological response). (b) Average BR thresholds and preferred direction across 10 animals. (c) Average laryngeal EMG thresholds and preferred direction in 5 animals. (d) Average blood pressure threshold distribution in 2 animals. (H) (a) Average spatial distributions of normalized eCAP response amplitudes for fast fibers across animals. Contact with greatest fiber response amplitude is placed at 12 o’clock direction and corresponds to the outer circle; origin of the plot represents the minimum response amplitude for each animal. p value represents statistical significance of 1-way ANOVA (dependent variable: fiber response amplitude, independent variable: direction of contact). (b) Same as (a), but for slow fibers.

Discussion

In this study we demonstrate rich, functionally and translationally relevant structure in the arrangement of fibers and fascicles within the cervical and thoracic vagus nerve in swine. We chose the swine model because the vagus resembles the human vagus in its fascicular structure. It is also a closer overall fit to the human vagus compared to other experimental species, including rodents and non-human primates [1, 3]. The swine and human vagus nerves have with similar effective nerve diameter and relative thickness of endoneurium, perineurium and epineurium [3]. The swine vagus has 10 times more fascicles than the human vagus and accordingly smaller diameter fascicles (Suppl. Figure 1). Since activation profiles of vagus fibers are largely determined by their distance from the stimulating electrode and the morphology of the surrounding tissues, the swine vagus may provide a testbed for spatially selective neuromodulation that is potentially even more challenging than in humans.

The vagus nerve extends branches to numerous organs through its descent from the brainstem down to the abdomen, for sensory and motor innervation. The pharyngeal branches, superior laryngeal nerve, recurrent laryngeal nerve, and the superior cardiac nerve are the four branches of the vagus nerve within the neck [1, 45]. The vagus nerve continues into the chest and abdomen where it innervates the heart, tracheobronchial tree, lungs, esophagus, stomach, pancreas, liver, and gastrointestinal tract via numerous branches. Though variability in the branching pattern has been observed at the nodose and cervical level of the vagus in humans and pigs [1, 45], the overall branching pattern to the visceral organs remains consistent between subjects ([3, 46], Suppl. Table 1). Vagus branches are formed from fibers that descend in the trunk along fascicles and are surrounded by perineurial structures [3, 46]. Our finding that primarily motor and primarily sensory fascicles form separate clusters in the cervical vagus (Figure 2) is consistent with a recent report describing clustering of fascicles with motor axons to laryngeal muscles in the swine cervical vagus [1]. In the context of organ-specific organization of the nerve, the larynx is just one of the several organs represented in separate, organ-specific fascicle clusters (Figure 1).

Our findings raise the exciting possibility of viscerotopic arrangement of fibers in the trunk of the vagus, in a similar manner to the somatotopic organization of other peripheral nerves (e.g. [1]. In the context of organ-specific organization of the nerve, the larynx is just one of the several organs represented in separate, organ-specific fascicle clusters (Figure 1). Our findings raise the exciting possibility of viscerotopic (or organotopic) arrangement of fibers in the trunk of the vagus, in a similar manner to the somatotopic organization of other peripheral nerves (e.g. [6]). Topographic organization of motor vagus neurons has been described in the dorsal motor nucleus (DMV) of the brainstem , with specific organs occupying distinct locations [47, 48]. A total of nine sub-sections have been identified in the DMV and are grouped into three divisions; rostral representing the abdominal organs, intermediate representing the esophagus, and tracheal and caudal representing the cardiac [49]. Sensory vagus neurons are also viscerotopically organized. For example, cells in the NG projecting to the soft palate and pharynx are clustered superiorly, and those projecting to the esophagus and stomach are located inferiorly [50]; sensory inputs to the nucleus tractus solitarius (NTS), the main sensory vagus nucleus in [49]. Sensory vagus neurons are also viscerotopically organized. For example, cells in the NG projecting to the soft palate and pharynx are clustered superiorly, and those projecting to the esophagus and stomach are located inferiorly [50];

[49]. Sensory vagus neurons are also viscerotopically organized. For example, cells in the sensory nodose ganglion projecting to the soft palate and pharynx are clustered superiorly, and those projecting to the esophagus and stomach are located inferiorly [50]. Sensory inputs terminate in a viscerotopic manner in the nucleus tractus solitarius (NTS), the main sensory vagus nucleus in the brainstem [51-53]; visceral afferent projections from the NTS to higher brain centers, relayed through the parabrachial nucleus and the nucleus reticularis rostroventrolateralis are also topographically organized [54-57]. In the vagus trunk,

bronchopulmonary and laryngeal fascicles merge soon after they join the trunk (Figure 1), whereas a portion of the cardiac cluster does not merge with other fascicles (Figure 1). Organ-specific fascicles gradually merge in the rostral to caudal direction. The sensory-motor fascicle separation is maintained throughout the cervical vagus (Figure 2) and disappears in the thoracic vagus (Suppl. Figure S10). Based on these findings, mid- or lower-cervical placement of bioelectronic devices may provide means for organ- and function-selective neuromodulation.

A second layer of neural organization in the vagus involves several anatomically- and functionally-distinct fiber types. Large myelinated efferents (Aα-type) provide somatic innervation to laryngeal muscles [58, 59] and smaller ones (B-type) represent parasympathetic regulation to visceral organs, like heart [59]. Large myelinated afferents (Aβ -type) provide somatic sensation to the pharyngeal and laryngeal mucosa [24-26], whereas smaller ones (Aδ-type) project to autonomic sensory receptors in viscera [31-34]. Unmyelinated C-type efferents represent primarily sympathetic fibers to visceral organs [23, 30, 35], whereas unmyelinated C-type afferents mediate visceral sensation [25, 32, 33, 39]. The human and swine vagus contains fibers of all these types [2, 12, 13]. Historically, researchers have relied on electron microscope imaging methods to quantify fiber numbers and fiber types in peripheral nerves, including the vagus. Fiber types were largely differentiated as myelinated or unmyelinated fibers using rigorous annotations of thousands of photographed images done manually. To differentiate between non-myelinated efferent fibers from the afferent fibers, researchers in the past first quantified the total number of fibers in an intact vagus nerve, then compared the fiber numbers to vagotomized animals, where vagotomy was performed in the supra nodose region of the nerve [46, 60]. Supra nodose vagotomy would selectively cause degeneration of the efferent fibers but not the afferent fibers, as the cell bodies of the sensory fibers are predominantly located in the nodose ganglion. The vagus nerve with degenerated efferent fibers was termed sensory vagus [60]. Quantification of fibers in the was then achieved by selecting random regions of the nerve which were sampled and imaged with an electron microscope, an area of about 1:10 – 1:20 of the total surface of the nerve [60]. The number of fibers in the sampled area was counted manually and the values were extrapolated to reflect the total number of fibers in the entire nerve area. Fiber count in the sensory vagus reflected afferent fibers, which was further differentiated to myelinated or non-myelinated afferent fiber count. The difference in the fibers count between sensory vagus and intact vagus reflected the total number of efferent fibers in the vagus nerve. Though survival surgeries with selective ablation experiments are possible in rodents, domesticated cats, and ferrets, such experiments are not possible in humans and large animals such as pigs. Also due to the arduous nature of the surgical technique, there is a high chance for spared axons to be present due to incomplete ablation that will lead to incorrect afferent fiber count. Variation in the surgical technique from animal to animal along with incomplete degeneration of the efferent fibers after ablation can increase the number of false-positive afferent fiber count in the sensory vagus. Furthermore, since fiber distribution inside the nerve and not even inside a fascicle is distributed evenly, fiber count in the selective region of a fascicle won't reflect the actual count for a given fiber type. Since the counts were also performed manually in thousands of the photographed electron microscope images, there was an increased chance for human error in the quantification process.

To address the above-mentioned issues, we developed a quantitative anatomy pipeline for staining, imaging, identification and quantification of fibers. Antigen expressed by certain fiber types can be selectively targeted using a specific antibody tagged to a fluorophore. Since antibody binding is highly sensitive and selective only to a particular antigen, multiple antibodies with different fluorophore wavelengths can be used to identify several antigens at the same time with greater precision. For instance, in our study we used an antibody against choline acetyltransferase (ChAT), neurofilament (NF) and myelin basic protein (MBP) colocalize together to identify large MEff fibers, and the fibers that lacked ChAT staining but positive for NF and MBP were classified as myelinated efferents. Fibers that lacked ChAT and MBP were classified as unmyelinated efferents. Using an antibody against Nav1.8, a tetrodotoxin (TTX)-resistant voltage-gated channel encoded by

the SCN10A gene that is expressed specifically by small afferent fibers, we identified clusters of fibers that were classified as unmyelinated afferents. Since non-myelinated Schwann cells called Remak Schwann cells are known to encompass small unmyelinated fiber clusters, we further confirmed the accuracy of detecting C-afferent clusters by co-localizing them with the S100 antibody expressed by the Schwann cells (Figure 3B). To the best of our knowledge, this is the first methodology that allows quantification of small, unmyelinated fibers using light microscopy. Previously, ChAT expression was quantified using a DAB chromogen technique, and the slides were imaged at 20x magnification [1]. In this work, we employed immunofluorescence (IF) to detect ChAT expression. The advantage of using the IF technique is the ability to colocalize the ChAT expression with NF and Myelin basic protein. Also, IF enabled us to visualize individual fibers at 100 x high magnification with the subcellular localization of the ChAT, NF, and MBP in the same axon with high selectivity and sensitivity, which is not possible using the DAB chromogen technique. Axons expressing ChAT, NF, and MBP were identified as efferent fibers. Similarly using the IF technique, we identified afferent fibers that are selectively positive for Nav1.8 but negative for NF and MBP. This is a novel way to differentiate efferent fibers from afferent fibers that was not possible using the DAB chromogen technique. Measurement of the diameter of single fibers allowed us to further classify them into additional sub-types (Figure 3, table I). In our study we imaged the entire nerve and all fascicles at a resolution of 0.150 microns/pixel. At that resolution, individual axons as small as 0.3 micron diameter can be visualized and measured. The immunofluorescence technique in combination with the automated algorithm to efficiently analyze very large image sets provides unprecedented quantification of whole populations of fibers in large peripheral nerves.

Using the pipeline, we were able to count, rather than estimate, all fibers in the vagus nerve (Table I). Previous studies in cats, ferrets, rats, and humans have shown approximately 80% of the fibers in the cervical vagus nerve are unmyelinated fibers but such quantification hasn't been done in swine. Also, the distinction of the myelinated and unmyelinated fibers to either afferent fiber or efferent fibers has been limited only to cats and ferrets. Quantification of unmyelinated afferent fibers have been shown to around be 78.8 % in ferrets and 53.3.6% in cats, and the number of unmyelinated efferent fibers to be 7.9% in ferrets and 26.2% in cats. Similarly, here we report, the percentage of the unmyelinated afferent fibers to be 81.70% in the left cervical vagus nerve (LCVN) and 83.25% in the right cervical vagus nerve (RCVN), and the percentage of unmyelinated efferent fibers to be 5.65% in LCVN and 4.47 % in the RCVN. The number of myelinated afferent fibers was reported to be approximately 9% both in cats and ferrets consistent with our results that show myelinated afferent fibers approximately 8.79% in the LCVN and 8.13% in the RCVN in pigs. Myelinated efferent fibers were reported to be 4.1% in ferrets, a close match to our findings in pigs where we report 3.85% in the LCVN and 4.15% in the RCVN. In conclusion, our results indicate the distribution of vagal fibers in pigs is consistent with previously published data in ferrets and with a slightly lower proportion of myelinated efferents and unmyelinated efferents in comparison to cats.

The presence of small, unmyelinated adrenergic fibers in the cervical and sub-diaphragmatic vagus nerve has been well documented in rats ([20] , cats [21] dogs [22], and humans [23]. The combined vagus nerve and sympathetic trunk, termed the "vagosympathetic trunk", has been shown to exist in dogs and cats [27] [28]. However, in humans, the vagus nerve and sympathetic trunk are separated anatomically, although recent evidence suggests hitchhiking branches within the vagus nerve project from the cervical sympathetic chain [29]. The quantification and distribution of adrenergic fibers within the vagus nerve have been shown to vary between species, possibly due to variation in both in the number of fascicles and the relative size of the vagus nerve between species [1]. In dogs, tyrosine hydroxylase positive (TH+) fibers occupied up to 2.8 % of the cross section of the vagus nerve and were distributed mainly in the periphery of the nerve at the cervical region, while TH+ fibers were scattered throughout the periphery *and* center of the nerve at the thoracic levels [22]. In humans, sympathetic nerve fibers are present throughout the vagal trunk at the cranial level, jugular ganglion, nodose ganglion, cervical level, thoracic trunk, and all of the vagal branches, including the superior

laryngeal, superior cardiac, recurrent laryngeal, inferior cardiac, pulmonary and esophageal branches [30]. At the cervical level, the sympathetic fibers have a diffuse distribution pattern in humans [30], occupying up to 21.63% of the total cross-section at the cervical and thoracic level, with similar amounts in both the left and right side [35]. Using combined immunocytochemistry and retrograde injections in the subdiaphragmatic vagus nerve of rats, it has been shown that the majority of the cell bodies of adrenergic fibers projecting to the vagus nerve were located at the dorsal motor nucleus (75%) and nodose ganglia (17%), and only few fibers projected from the postganglionic sympathetic neurons (8%) [20]. This suggests that sympathetic innervation in the vagus nerve is derived primarily from the parasympathetic source [20] . Though, the role of the sympathetic fiber in the vagus nerve is still not well understood, it has been found that majority of the TH+ fibers surround the ChAT neurons in the DMV, with few neurons expressing both ChAT and TH [36]. This suggests that vagus nerve is composed of both catecholaminergic and cholinergic fibers. Quantification and distribution of adrenergic fibers in the pig vagus nerve has not been reported. Here we show that 5% of the small unmyelinated fibers in the cervical vagus nerve are negative for sensory fiber marker Nav1.8 but positive for neurofilament. Given the similarity of the pig vagus nerve to humans, majority of these unmyelinated fibers could be post ganglionic sympathetic motor fibers. In addition, there is a possibility that small percentage of these unmyelinated fibers in the vagus nerve could be the non-adrenergic non-cholinergic (NANC) fibers. As It has been shown that majority of inhibitory NANC input to the trachea is projected though recurrent laryngeal nerve, this suggests the existence of NANC fibers within the vagus nerve [37].In a previous study, ChAT expression was quantified using a DAB chromogen technique, and the slides were imaged at 20 x magnification [1]. In this work, we employed immunofluorescence (IF) to detect ChAT expression. The advantage of using the IF technique is the ability to colocalize the ChAT expression with NF and Myelin basic protein. Also, IF enabled us to visualize individual fibers at 100 x high magnification with the subcellular localization of the ChAT, NF, and MBP in the same axon with high selectivity and sensitivity, which is not possible using the DAB chromogen technique. Axons expressing ChAT, NF, and MBP were identified as efferent fibers. Similarly using the IF technique, we identified afferent fibers that are selectively positive for Nav1.8 but negative for NF and MBP. This is a novel way to differentiate efferent fibers from afferent fibers that was not possible using the DAB chromogen technique.

The use of multi-contact electrodes for current steering is the standard method to deliver spatially selective nerve stimulation, as it permits the targeting of a sub-set of fascicles or fibers. This approach was demonstrated in a rat model of VNS, in which reduction of blood pressure was attained without affecting heart rate and breathing rate [61]. It was also used in a sheep model of VNS, in which fascicular stimulation attained changes in breathing rate without affecting the heart rate [16]. Ours is the first demonstration of spatially selective VNS in the swine model, and the first report of a chronic VNS implant in swine (Suppl. Figure S20). Given the relevance of the swine model to human VNS, our results indicate that the use of cuff electrodes, which minimize the risk of injury compared to intraneural electrodes, are a viable solution for organ- and function-specific vagus neuromodulation.

Methods

Animal surgeries

The effects of VNS on physiological and neural response were examined in male pigs (Yucatan; n=13, ~50kg; Yorkshire, n=1, ~30 kg). All of the animal protocols and surgical procedures were reviewed and approved by the animal care and use committee of Feinstein Institutes for Medical Research and New York Medical College.

Anesthesia: For a 12-hour period before surgery, the animals were maintained on a no food and no fluid regimen (NPO). On the day of surgery, the animals were weighed and sedated with mixture of Ketamine (10-20 mg/kg) and Xylazine (2.2 mg/kg) or Telazol (2-4 mg/kg). Propofol (4-6 mg/kg, i.v.) was used to induce anesthesia, and following intubation, the anesthesia will be maintained with isoflurane (1.5-3%, ventilation). Mechanical ventilation will be provided and might be turned off to measure the breathing change during VN stimulation. Animals were placed on a table in a supine position with normal body temperature between maintained between 38°C and 39°C using a heated blanket and/or a hot air warmer and monitored with a rectal probe thermometer. Blood pressure and blood oxygen level were monitored with a BP cuff and a pulse oximeter sensor. The depth of anesthesia was monitored by assessing heart rate, blood pressure, respiration, and mandibular jaw tone. All surgeries were performed using sterile techniques.

For survival surgeries, a fentanyl patch (25-50 mcg/hr) and buprenorphine (0.01 mg/kg s.q.) were provided to the animal at the end of surgery to alleviate post-operative pain. After gradually weaning off the ventilator and extubated and when physiological signs returned to normal, animals were returned to the home cage and were monitored 3 times/day for 72 hours. Cefazolin (25 mg/kg p.o.) was given for 5 days. Carprofen (2-5 mg/kg, s.q.) was administered when the animal showed signs of pain. Animals were allowed 10 days for full recovery before any tests were performed.

Physiology experiments

Breathing rate: Breathing was monitored by using a respiratory belt transducer (TN1132/ST), which was placed around the belly or chest and connected to a bridge amplifier (FE221, ADI). The change of the belt pressure with breathing represented the breathing cycle and was used to derive the breathing rate. The mechanical ventilator was turned off when measuring the effects of vagus nerve stimulation on breathing.

ECG: The skin around the wrist was shaved and conductive gel was applied to patch electrodes which were subsequently adhered to the skin, ECG was recorded using a 3-lead patch electrode configuration and amplified using a commercial octal bio-amplifier (FE238, ADI).

Heart blood pressure: Ultrasonic guidance (H8018QE and Vivid iq v203 4D) was used to pass a 19 G angiographic needle through the skin at a 60-degree angle to the target vessel. Once blood backflow was detected, a soft guidewire (0.035 inches) was introduced into the vessel. A 5-Fr micro manometer-tipped catheter (SPR-751, Millar Inc) was advanced into the aorta or right ventricle, and pressure was recorded continuously after amplification (FE228 ADInstruments). The catheter locations were confirmed by verifying the characteristic phasic blood pressure waveforms corresponding to different placements.

All physiological signals were first digitized and then acquired at 1 kHz (PowerLab 16/35, ADI) and then visualized using LabChart (ADInstruments Inc).

Cervical vagus nerve implant and recording

Under the surgical level of anesthesia, a 4-5 cm long incision was cut down to the subcutaneous tissue on the right or left cervical region of the neck, 2 cm lateral to the midline. Subcutaneous tissues were dissected and retracted to expose the underlying muscle layers. The sternomastoid muscle was bluntly separated and retracted laterally away from the surgical field. The carotid sheath was exposed and the vagus nerve was identified and isolated away from the carotid artery. One or two 8-contact cuff electrodes (CorTec Inc) were placed on the rostral (around 2cm to nodose) and/or caudal sites with a distance of 4 to 5 cm after isolating the underlying 2 cm long section for each electrode. The middle portion, between the two isolated sites was left intact within the carotid bundle to minimize the extent of surgical manipulation and trauma to the nerve. For laryngeal muscle recording, after the hyoid bone was blunt dissected, Telfon-insulated single or multi-stranded stainless-steel wires were de-insulated at the tip about 1 mm, and inserted in thyroarytenoid (TA) of laryngeal muscle with a needle. For survival surgery, the incision was closed, the leads and connectors of the implanted cuff electrodes and EMG electrodes are tunneled from the surgical field in the neck area to the back of the neck subcutaneously and then to the top of the skull, where they are externalized. Several stainless-steel skull screws are implanted in the exposed area of the skull by drilling small burr holes. The connectors and the anchoring screws are secured with dental acrylic, and then a titanium casing will be attached around and secured to the skull around the connector for protection of the implants.

Neural signal and EMGs were sent to the data acquisition system through a headstage (RHS 32, Intan Tech). It was filtered (60-Hz notch), amplified, and digitized at a sampling frequency of 30 kHz with an acquisition system (Intan 128 recording/stimulating, Intan Tech).

Paradigms of vagus nerve stimulation and physiological data analysis

Physiological thresholds: Vagus nerve stimulation was found to modulate different physiological responses, and different functional fascicles were found to show topo-organizations within the nerve. Biphasic stimulus pulses were delivered through an isolated constant current stimulator (STG4008, Multichannel Systems). Physiological threshold (PT) was detected from stimulus trains of 10 s durations (30 Hz, pulse width 200 μs). There was at least 30 s long duration between successive trains to ensure that physiological measurements had reached a steady state before a new train was delivered. We define PT as the lowest stimulation intensity to induce 5% drops of HR, and 50% drop of BR as the thresholds for HR and BR, respectively. In awake animals we tested PT of cough, which is the lowest stimulation to induce coughing. The threshold of EMG was the lowest intensity to induce a visible response. The thresholds for each of the eight contacts were tested randomly.

Evoked compound action potential(eCAP): After removing the DC component (<1 Hz) from recordings, evoked compound action potentials (eCAP) from the vagus nerve were averaged across all of the individual stimulus pulses within each train. The responses (peak-to-peak) from eCAP within predefined time window were classified into different fibers based on the conduction speed. Given the distance between recording and stimulation electrode ~50 mm, the first peak latency within 1.5 ms (conduction speed, >33 m/s) was classified as a fast fiber response, and the late peak after the 2 ms was classified as slow fiber response (conduction speed, <25 m/s). In most of the recordings, EMG contamination observed in eCAP recordings could be blocked by Vecuronium. Long latency C-fiber response was not observed in our tests. The eCAP responses (peak-to-peak amplitude) from eight contacts on the second cuff were recorded simultaneously while stimulating each of the eight contacts.

Recruitment map and population responses: The responses from laryngeal muscle (peak-to-peak EMG amplitude), breathing rate change and mean eCAPs responses (8 contacts) of different fibers were characterized to inform recruitment maps during increasing stimulation intensity across 8 stimulating contacts.

To characterize the spatial selectivity of the 8-contact cuff, PTs and eCAPs from each contact were plotted on a polar-plot with mean direction and resultant vector length. To show the spatial selectivity across animals and compare difference between physiological responses, we aligned the lowest thresholds of HR on the 12 o'clock position from all animals, and then PTs of BR and EMG was aligned to the HR. Then the PTs were normalized between the lowest (to 0) and highest (to 1) to give the population (mean+/- SE) across animals. Similarly, we first aligned the highest responses (eCAP of peak-to-peak amplitude) of fast fiber to 12 o'clock position, and then we get the population eCAPs (mean+/- SE) across all animals, and finally the population response from slow fiber eCAPs were alighted to the fast response for each pig and averaged across animals (mean+/- SE). ANOVA was used to test the spatial selectivity across contacts (anova1, *$p<0.05$).

Euthanasia

At the end of the study, the swine was euthanized with a solution (Euthasol) (A dosage of 1 ml/10 pounds BW, i.v.). Euthanasia solution (Euthasol) was injected intravenously. Death was confirmed using the ECG signal and the arterial blood pressure signal. Absence of a pulse in both signals confirmed cardiac death. After euthanasia, both the left and right vagus nerve were harvested for histology.

Micro-Computed Tomography

Pigs were euthanized, and the cervical vagus nerve from both the left and right side were carefully dissected and fixed in 10% formalin for 24 hours. The nerve samples were transferred to Lugol's solution (Sigma, L6146) for five days before the micro-CT scan to achieve optimal fascicular contrast. Nerve samples were wrapped in a less dense material such as saran wrap and mounted in position on a vertical sample holder tube. The samples were scanned using Bruker micro-CT skyscan 1172 with a voxel size of 6 μm resolution. Volume rendering was done using Bruker CTvox v3.3.1 to obtain a 3D reconstructed view of the nerve (Suppl. Figure S2-S4).

Micro-Computed Tomography Tracking of Fascicles

The automated fascicle tracing approach consists of two stages: detection and tracking. We chose a mask RCNN model as our detector because it performs well on the detection task and can readily be updated in individual animals if necessary. The model was trained on 6000 (out of 7500) cross-sectional micro-CT images of a vagus nerve that were manually labeled. The tracker filters and structures the detections to construct a graph that captures properties of the fascicular cross-sections (shape and texture metrics) at each node and encodes branching and merging via the graph edges. Trackers can improve the overall performance by delaying decisions while accumulating evidence so that low-contrast fascicular segments can be discerned, and by constraining the motion of the fascicular branches as they traverse longitudinally. Individual fascicles contributing to the different vagal branches were manually identified at the branching points (Suppl. Figure S2-S4). The tracked fascicle trajectories were then color coded from the caudal end of the branching point to the rostral end of the nodose ganglion (Figure 1).

Immunohistochemistry

Cross-section of the vagus nerve at 5 μm thickness was obtained through paraffin sectioning. Sections were stained for myelin basic protein (MBP), NF, choline acetyltransferase (ChAT) and Nav1.8 using standard IHC protocol [62] to identify the number and distribution of the myelinated and non-myelinated fibers inside different fascicles. Briefly, sections were subjected to deparaffinization procedure using xylene and ethanol rinse and then washed with distilled water for 10 min. Antigen retrieval was performed by briefly subjecting the samples to 1 x citrate buffer to unmask the antigens. Sections were rinsed with 1x Tris-buffered saline and subjected to 1 hour of blocking step using one normal goat serum. Sections were incubated with anti-Neurofilament (1:500, Abcam AB8135), anti- Myelin basic protein (1:500, Abcam AB7349), anti-ChAT (Millipore Sigma, AB144P), and SCN10A Monoclonal Antibody (Nav1.8, MA5-27663 Fisher) overnight at 4 °C in a shaking humidifier. The

following day, sections were rinsed and incubated with the secondary antibody for two hours at room temperature. Slides were then rinsed thoroughly with TBS buffer three times, and cover glass was mounted on the sides with the fluoromount (Vector labs, H-1700). The slides were then imaged using ZEISS LSM 900, confocal laser scanning microscope, and BZ-X800 all-in-one fluorescence microscope at 100x magnification.

Fiber segmentation and feature extraction

We designed a set of algorithms and a data pipeline to segment and extract nerve, fascicle and single-axon level features from IHC images of the vagus. First, we developed a fiber segmentation and feature extraction algorithm by combining standard computer vision methods with statistical modeling and geometrical manipulations, including Gaussian mixture models and Voronoi tessellation, and achieved a single-axon detection accuracy of 82% and myelination classification accuracy of 89% [63]

To improve the detection accuracy, we further trained a Mask R-CNN deep convolutional neural network on axon instance segmentation. The model was pretrained on the COCO Instance Segmentation task [64]. We generated training images by first annotating fibers using the more standard algorithm, followed by manual correction of 80 fascicles, done in an ordinary image editing software. We estimated that pre-annotating using the original algorithm reduced the time of correction by four times compared to manual annotation from scratch.

Fiber Detection

Neurofilament: To detect neurofilament positive pixels, we empirically selected a threshold brightness in the neurofilament color channel (154 out of 256) above which pixels were classified as positive. We further discovered connected components of such pixels to arrive at blobs of neurofilament. Blobs containing less than 10 pixels were excluded as noise. The remaining blobs were broken divided into individual fibers by fitting Gaussian mixture model on them of different number of Gaussian distributions (i.e. number of fibers) and then selecting the best fit determining the amount and location of enclosed axons.

Myelin: Myelin positive pixels were detected using the same technique as described previously [63]. Briefly myelin channel pixels surrounding each detected neurofilament positive axon were analyzed. Pixels were classified as myelin positive when their brightness reached 128 out of 256. First, the outside pixel shell of neurofilament positive fibers were taken and neighboring pixels were recursively checked (for a maximum of 5 recursive steps) for myelin positive pixels. If more than 30% of fiber neighboring pixels were found to be myelin positive, the said fiber was classified as myelinated.

ChAT: Similar to Neurofilament and myelin pixel classification, we empirically selected a brightness threshold, applied to the chat color channel, of 131 out of 256. Chat positive pixels overlapping myelinated axons were counted separately for each fiber and if more than 5% of pixels were found to be chat positive, we regarded the fiber as chat positive.

The final set of segmentations was performed by the combination of the standard computer vision and deep learning algorithms: we let Mask R-CNN detect axons first, then opted for traditional methods to detect and divide overlapping neurafilament blobs that were ignored by the deep learning model. This combination achieved a fiber detection accuracy of 96% [65]

After the instance segmentation of neurafilament and the assignment of myelin to detected fibers, we extracted a set of features for each axon. These features include the longer and shorter diameters, the perimeter, and area of the fiber, in addition to the thickness of the myelin, and the polar coordinates of the fiber relative to the center of mass of the enclosing fascicle.

We manually annotated nerve cross-sections on the fascicle level to derive polar coordinates of fascicles and their distance from the epineurium. Moreover, we extracted fascicle-level features including the perimeter of

the perinerium, the area of the fascicle enclosed by the perinerium, and the total count and area of each fiber type within a fascicle.

Nav1.8: Similar to generate ground truth for the deep learning instance segmentation network, we performed manual annotation of NAV1.8 stained images to determine the density of C fibers within bundles given the area of the enclosing bundle. Due to the low resolution of light microscopy at the range of 1 µm, we used Airyscan equipped super high resolution confocal microscope captured laser microscopy images of parts of fascicles, from which single NAV1.8 positive C fibers can be distinguished (Suppl. Figure S11, a). These high resolution images were manually annotated bundle-by-bundle to amass counts of fibers within more than 300 bundles extracted from two animals and four different fascicles. To predict number of NAV1.8 positive C fibers from lower resolution light microscopy images (Suppl. Figure S11, c) a linear regression model was fit on the C fiber counts given the area of the bundle (R^2 = XY) (Suppl. Figure S11, d). We subsequently employed the linear regression model to estimate the number of NAV1.8 positive C fibers in clouds of NAV1.8 stains, detected as bundles, in light microscopy images (Suppl. Figure S11, e). As the linear regression model estimates are real numbers, we round those numbers to the closest integer for each detected bundle to get actual counts.

All images are preprocessed before the segmentation to enhance contrast and to remove noise. Myelin-neurafilament-chat-stained images were first adjusted by adaptive histogram equalization (dividing each fascicle image into a 32-by-32 grid), then color clipped by defining upper and lower threshold of the clip for separately each cross section manually. The thresholds for each cross-section and channel were selected to remove background noise and to render the stains close to binary (distinct foreground and background), which removed the brightness variance between cross-sections allowing us to use the same parameters for all cross-sections in the subsequent segmentation process. NAV1.8 images were not processed by adaptive histogram equalization, but were color clipped as described above. In the subsequent segmentation process, we ignore all individual neurafilament and NAV1.8 blobs that are smaller than 0.225 um^2, which we found to be background noise rather than actual fibers.

Data analysis

Once we detected and localized fibers and fascicles, and further extracted features from them, we performed subsequent analysis to map the distribution of different fiber types within-fascicle, and within the whole nerve.

We calculated within-fascicle counts and areas of the four fiber types, namely, myelinated efferents (MEff), myelinated afferents (MAff), unmyelinated efferents (UEff) and unmyelinated afferents (UAff). The per-fascicle counts are either presented in their absolute values (Figure 3A, I-L) or as percentages normalized by the total fiber count per fascicle (Figure 3C).

For each fiber type we estimated the ratio of its neighboring fiber types in a 15 µm radius (Figure 3E, c). For each fiber in every fascicle at the mid-cervical level, we captured its neighboring fibers using k-nearest neighbors, then filtered out the ones outside of the 15 µm radius of the fiber. We accumulated the counts of neighboring fiber types for each center fiber type; normalized by the total count of neighbors we calculated the overall ratio of a fibers a given type being in the neighborhood of a given fiber type. To further describe the tendency of different fiber types to share space, we compared their total numbers in each fascicle (Figure 3D, a & b). Within-fascicle mixing was analyzed by splitting each mid-cervical fascicle into a grid of 30-by-30 µm non-overlapping spatial sectors, establish the fiber counts by type in the sectors, then finally count the number of sectors of a certain composition and represent the propensity of two fiber types to share a space of 30-µm-width fascicle area by showing a 2D histogram of the distribution of compositions of the two fiber types (Figure 3E, a & b)

To examine distribution of fiber types within the nerve, we measured the percentage of a fiber type being positioned in fascicles inside rings of 100-µm width at different distances from the epinerium. We show the

overall distribution of fiber types as the function of epinerium distance combining data extracted from nerves of different animals at the mid-cervical level (Suppl. Figure S14, A). We also present the same information for individual nerves as cumulative distributions (Suppl. Figure S15). We grouped fascicles according to their effective diameter into 50 -µm bins and measured the percent area occupied by each fiber type within each fascicle normalized by the area of the fascicle. We then computed the average and standard deviation of such fiber type percentages per effective diameter bin (Suppl. Figure S14, B).

As we manually annotated single fibers of MEff, MAff, UEff and UAff to generate ground truth data for our instance segmentation and NAV1.8 positive C fiber counting model, we had access to accurate single-fiber features. To gauge the size of the different fiber types, we measured the effective diameter of the manually annotated single fibers of each type and presented their distribution (Suppl. Figure S12).

References

1. Settell, M.L., et al., *Functional vagotopy in the cervical vagus nerve of the domestic pig: implications for the study of vagus nerve stimulation.* J Neural Eng, 2020. **17**(2): p. 026022.
2. Stakenborg, N., et al., *Comparison between the cervical and abdominal vagus nerves in mice, pigs, and humans.* Neurogastroenterol Motil, 2020. **32**(9): p. e13889.
3. Pelot, N.A., et al., *Quantified Morphology of the Cervical and Subdiaphragmatic Vagus Nerves of Human, Pig, and Rat.* Front Neurosci, 2020. **14**: p. 601479.
4. Thompson, N., S. Mastitskaya, and D. Holder, *Avoiding off-target effects in electrical stimulation of the cervical vagus nerve: Neuroanatomical tracing techniques to study fascicular anatomy of the vagus nerve.* J Neurosci Methods, 2019. **325**: p. 108325.
5. Kenny, B.J. and B. Bordoni, *Neuroanatomy, Cranial Nerve 10 (Vagus Nerve)*, in *StatPearls*. 2021: Treasure Island (FL).
6. Stewart, J.D., *Peripheral nerve fascicles: anatomy and clinical relevance.* Muscle Nerve, 2003. **28**(5): p. 525-41.
7. De Ferrari, G.M., et al., *Long-term vagal stimulation for heart failure: Eighteen month results from the NEural Cardiac TherApy foR Heart Failure (NECTAR-HF) trial.* Int J Cardiol, 2017. **244**: p. 229-234.
8. Sinniger, V., et al., *A 12-month pilot study outcomes of vagus nerve stimulation in Crohn's disease.* Neurogastroenterol Motil, 2020. **32**(10): p. e13911.
9. Doko, I., et al., *[Vagal Nerve Stimulation in the Treatment of Patients with Rheumatoid Arthritis - Results through Day 84 Obtained at the Croatian Center of an International Pilot Study].* Reumatizam, 2016. **63**(2): p. 1-8.
10. Giordano, F., et al., *Vagus nerve stimulation: Surgical technique of implantation and revision and related morbidity.* Epilepsia, 2017. **58 Suppl 1**: p. 85-90.
11. Nicolai, E.N., et al., *Sources of off-target effects of vagus nerve stimulation using the helical clinical lead in domestic pigs.* J Neural Eng, 2020. **17**(4): p. 046017.
12. Hoffman, H.H. and H.N. Schnitzlein, *The numbers of nerve fibers in the vagus nerve of man.* Anat Rec, 1961. **139**: p. 429-35.
13. Pelot, N.A. and W.M. Grill, *Effects of vagal neuromodulation on feeding behavior.* Brain Res, 2018. **1693**(Pt B): p. 180-187.
14. Musselman, E.D., N.A. Pelot, and W.M. Grill, *Empirically Based Guidelines for Selecting Vagus Nerve Stimulation Parameters in Epilepsy and Heart Failure.* Cold Spring Harb Perspect Med, 2019. **9**(7).
15. Fitchett, A., S. Mastitskaya, and K. Aristovich, *Selective Neuromodulation of the Vagus Nerve.* Front Neurosci, 2021. **15**: p. 685872.
16. Aristovich, K., et al., *Model-based geometrical optimisation and in vivo validation of a spatially selective multielectrode cuff array for vagus nerve neuromodulation.* J Neurosci Methods, 2021. **352**: p. 109079.
17. Erman, A.B., et al., *Disorders of cranial nerves IX and X.* Semin Neurol, 2009. **29**(1): p. 85-92.
18. Yuan, H. and S.D. Silberstein, *Vagus Nerve and Vagus Nerve Stimulation, a Comprehensive Review: Part I.* Headache, 2016. **56**(1): p. 71-8.
19. Weijs, T.J., et al., *Topography and extent of pulmonary vagus nerve supply with respect to transthoracic oesophagectomy.* J Anat, 2015. **227**(4): p. 431-9.
20. Yang, M., X. Zhao, and R.R. Miselis, *The origin of catecholaminergic nerve fibers in the subdiaphragmatic vagus nerve of rat.* J Auton Nerv Syst, 1999. **76**(2-3): p. 108-17.
21. Muryobayashi, T., et al., *Fluorescence histochemical demonstration of adrenergic nerve fibers in the vagus nerve of cats and dogs.* Jpn J Pharmacol, 1968. **18**(3): p. 285-93.
22. Onkka, P., et al., *Sympathetic nerve fibers and ganglia in canine cervical vagus nerves: localization and quantitation.* Heart Rhythm, 2013. **10**(4): p. 585-91.
23. Lundberg, J., et al., *Catecholamine-containing nerve fibres in the human abdominal vagus.* Gastroenterology, 1976. **70**(3): p. 472-4.
24. Djouhri, L. and S.N. Lawson, *Abeta-fiber nociceptive primary afferent neurons: a review of incidence and properties in relation to other afferent A-fiber neurons in mammals.* Brain Res Brain Res Rev, 2004. **46**(2): p. 131-45.
25. Mazzone, S.B. and B.J. Undem, *Vagal Afferent Innervation of the Airways in Health and Disease.* Physiol Rev, 2016. **96**(3): p. 975-1024.

26. Canning, B.J. and B.J. Undem, *Evidence that distinct neural pathways mediate parasympathetic contractions and relaxations of guinea-pig trachealis.* J Physiol, 1993. **471**: p. 25-40.
27. Reese, S. and C. Ruppert, *Ultrasonographic imaging of the vagosympathetic trunk in the dog.* Vet Radiol Ultrasound, 2001. **42**(3): p. 272-5.
28. Lee, L.Y. and T. Horikawa, *Development of alternating, ipsilateral Horner syndrome and Pourfour du Petit syndrome associated with oesophagostomy tube placement in a cat.* JFMS Open Rep, 2021. **7**(1): p. 2055116920984379.
29. Verlinden, T.J., et al., *Morphology of the human cervical vagus nerve: implications for vagus nerve stimulation treatment.* Acta Neurol Scand, 2016. **133**(3): p. 173-82.
30. Kawagishi, K., et al., *Tyrosine hydroxylase-immunoreactive fibers in the human vagus nerve.* J Clin Neurosci, 2008. **15**(9): p. 1023-6.
31. Belvisi, M.G., *Sensory nerves and airway inflammation: role of A delta and C-fibres.* Pulm Pharmacol Ther, 2003. **16**(1): p. 1-7.
32. Pavlov, V.A., S.S. Chavan, and K.J. Tracey, *Molecular and Functional Neuroscience in Immunity.* Annu Rev Immunol, 2018. **36**: p. 783-812.
33. Chang, R.B., et al., *Vagal Sensory Neuron Subtypes that Differentially Control Breathing.* Cell, 2015. **161**(3): p. 622-633.
34. Chen, S.L., et al., *Subdiaphragmatic vagal afferent nerves modulate visceral pain.* Am J Physiol Gastrointest Liver Physiol, 2008. **294**(6): p. G1441-9.
35. Seki, A., et al., *Sympathetic nerve fibers in human cervical and thoracic vagus nerves.* Heart Rhythm, 2014. **11**(8): p. 1411-7.
36. Cai, Q.Q., et al., *Distribution of dopamine receptors D1- and D2-immunoreactive neurons in the dorsal motor nucleus of vagus in rats.* Auton Neurosci, 2013. **176**(1-2): p. 48-53.
37. Moffatt, J.D., B. Dumsday, and J.R. McLean, *Characterization of non-adrenergic, non-cholinergic inhibitory responses of the isolated guinea-pig trachea: differences between pre- and post-ganglionic nerve stimulation.* Br J Pharmacol, 1999. **128**(2): p. 458-64.
38. Asala, S.A. and A.J. Bower, *An electron microscope study of vagus nerve composition in the ferret.* Anat Embryol (Berl), 1986. **175**(2): p. 247-53.
39. Kim, S.H., et al., *Mapping of Sensory Nerve Subsets within the Vagal Ganglia and the Brainstem Using Reporter Mice for Pirt, TRPV1, 5-HT3, and Tac1 Expression.* eNeuro, 2020. **7**(2).
40. Mata, M., D. Alessi, and D.J. Fink, *S100 is preferentially distributed in myelin-forming Schwann cells.* J Neurocytol, 1990. **19**(3): p. 432-42.
41. Harty, B.L. and K.R. Monk, *Unwrapping the unappreciated: recent progress in Remak Schwann cell biology.* Curr Opin Neurobiol, 2017. **47**: p. 131-137.
42. Grill, W.M., S.E. Norman, and R.V. Bellamkonda, *Implanted neural interfaces: biochallenges and engineered solutions.* Annu Rev Biomed Eng, 2009. **11**: p. 1-24.
43. Lotti, F., et al., *Invasive Intraneural Interfaces: Foreign Body Reaction Issues.* Front Neurosci, 2017. **11**: p. 497.
44. Ahmed, U., et al., *Implant- and anesthesia-related factors affecting cardiopulmonary threshold intensities for vagus nerve stimulation.* J Neural Eng, 2021. **18**(4).
45. Hammer, N., et al., *Human vagus nerve branching in the cervical region.* PLoS One, 2015. **10**(2): p. e0118006.
46. Havton, L.A., et al., *Human organ donor-derived vagus nerve biopsies allow for well-preserved ultrastructure and high-resolution mapping of myelinated and unmyelinated fibers.* Sci Rep, 2021. **11**(1): p. 23831.
47. Katz, D.M. and H.J. Karten, *Subnuclear organization of the dorsal motor nucleus of the vagus nerve in the pigeon, Columbia livia.* J Comp Neurol, 1983. **217**(1): p. 31-46.
48. Katz, D.M. and H.J. Karten, *Topographic representation of visceral target organs within the dorsal motor nucleus of the vagus nerve of the pigeon Columba livia.* J Comp Neurol, 1985. **242**(3): p. 397-414.
49. Huang, X.F., I. Tork, and G. Paxinos, *Dorsal motor nucleus of the vagus nerve: a cyto- and chemoarchitectonic study in the human.* J Comp Neurol, 1993. **330**(2): p. 158-82.
50. Broussard, D.L. and S.M. Altschuler, *Brainstem viscerotopic organization of afferents and efferents involved in the control of swallowing.* Am J Med, 2000. **108 Suppl 4a**: p. 79S-86S.

51. Berthoud, H.R. and W.L. Neuhuber, *Functional and chemical anatomy of the afferent vagal system.* Auton Neurosci, 2000. **85**(1-3): p. 1-17.
52. Gasparini, S., et al., *Central afferents to the nucleus of the solitary tract in rats and mice.* J Comp Neurol, 2020. **528**(16): p. 2708-2728.
53. Andresen, M.C. and D. Mendelowitz, *Sensory afferent neurotransmission in caudal nucleus tractus solitarius--common denominators.* Chem Senses, 1996. **21**(3): p. 387-95.
54. Kawai, Y., *Differential Ascending Projections From the Male Rat Caudal Nucleus of the Tractus Solitarius: An Interface Between Local Microcircuits and Global Macrocircuits.* Front Neuroanat, 2018. **12**: p. 63.
55. Herbert, H. and C.B. Saper, *Cholecystokinin-, galanin-, and corticotropin-releasing factor-like immunoreactive projections from the nucleus of the solitary tract to the parabrachial nucleus in the rat.* J Comp Neurol, 1990. **293**(4): p. 581-98.
56. Ross, C.A., D.A. Ruggiero, and D.J. Reis, *Projections from the nucleus tractus solitarii to the rostral ventrolateral medulla.* J Comp Neurol, 1985. **242**(4): p. 511-34.
57. in *The Role of the Nucleus of the Solitary Tract in Gustatory Processing*, R.M. Bradley, Editor. 2007: Boca Raton (FL).
58. Agostoni, E., et al., *Functional and histological studies of the vagus nerve and its branches to the heart, lungs and abdominal viscera in the cat.* J Physiol, 1957. **135**(1): p. 182-205.
59. Chang, Y.C., et al., *Quantitative estimation of nerve fiber engagement by vagus nerve stimulation using physiological markers.* Brain Stimul, 2020. **13**(6): p. 1617-1630.
60. Mei, N., M. Condamin, and A. Boyer, *The composition of the vagus nerve of the cat.* Cell Tissue Res, 1980. **209**(3): p. 423-31.
61. Gierthmuehlen, M., et al., *Haemodynamic Responses to Selective Vagal Nerve Stimulation under Enalapril Medication in Rats.* PLoS One, 2016. **11**(1): p. e0147045.
62. Zaqout, S., L.L. Becker, and A.M. Kaindl, *Immunofluorescence Staining of Paraffin Sections Step by Step.* Front Neuroanat, 2020. **14**: p. 582218.
63. Toth, V., et al., *Single-axon level automatic segmentation and feature extraction from immuhistochemical images of peripheral nerves.* Annu Int Conf IEEE Eng Med Biol Soc, 2020. **2020**: p. 1859-1862.
64. Yuxin Wu, A.K., Francisco Massa, Wan-Yen Lo and and Ross Girshick. , *Detectron2.* 2019.
65. Viktor Tóth, N.J., Adam Abbas, Moontahinaz Rob, Ariba Khan, Stavros Zanos, Theodoros P. Zanos *Single-axon level segmentation and feature extraction pipeline combining traditional and deep learning computer vision algorithms.* Abstracts from the Fourth Bioelectronic Medicine Summit:, 2020: p. P16. .